Spin Waves in Detwinned $BaFe_2As_2$

Xingye Lu,[1,*] Daniel D. Scherer,[2] David W. Tam,[3] Wenliang Zhang,[4] Rui Zhang,[3] Huiqian Luo,[4] Leland W. Harriger,[5] H. C. Walker,[6] D. T. Adroja,[6,7] Brian M. Andersen,[2,†] and Pengcheng Dai[3,1,‡]

[1]*Center for Advanced Quantum Studies and Department of Physics, Beijing Normal University, Beijing 100875, China*
[2]*Niels Bohr Institute, University of Copenhagen, Juliane Maries Vej 30, DK-2100 Copenhagen, Denmark*
[3]*Department of Physics and Astronomy & Rice Center for Quantum Materials, Rice University, Houston, Texas 77005, USA*
[4]*Beijing National Laboratory for Condensed Matter Physics, Institute of Physics, Chinese Academy of Sciences, Beijing 100190, China*
[5]*NIST Center for Neutron Research, National Institute of Standards and Technology, Gaithersburg, Maryland 20899, USA*
[6]*ISIS Facility, Rutherford Appleton Laboratory, Chilton, Didcot, Oxfordshire OX11 0QX, United Kingdom*
[7]*Highly Correlated Matter Research Group, Physics Department, University of Johannesburg, P.O. Box 524, Auckland Park 2006, South Africa*

(Received 16 April 2018; revised manuscript received 2 July 2018; published 8 August 2018)

Understanding magnetic interactions in the parent compounds of high-temperature superconductors forms the basis for determining their role for the mechanism of superconductivity. For parent compounds of iron pnictide superconductors such as AFe_2As_2 ($A = \mathrm{Ba}$, Ca, Sr), although spin excitations have been mapped out throughout the entire Brillouin zone, the respective measurements were carried out on twinned samples and did not allow for a conclusive determination of the spin dynamics. Here we use inelastic neutron scattering to completely map out spin excitations of ~100% detwinned $BaFe_2As_2$. By comparing observed spectra with theoretical calculations, we conclude that the spin excitations can be well described by an itinerant model when taking into account moderate electronic correlation effects.

DOI: 10.1103/PhysRevLett.121.067002

It is well known that high-temperature superconductivity in copper oxides and iron pnictides arises from electron and hole doping of their antiferromagnetically ordered parent compounds [1–4]. Since magnetism is believed to be important for superconductivity of these materials [1–6], it is therefore crucial to determine the magnetic interactions in the parent compounds in order to understand their evolution as a function of electron or hole doping. For insulating antiferromagnetic (AF) copper oxides such as La_2CuO_4, spin waves can be well described by a local-moment Heisenberg Hamiltonian [7,8]. In the case of metallic iron pnictides such as AFe_2As_2 ($A = \mathrm{Ba}$, Ca, Sr), a parent of iron-based superconductors, the material exhibits a tetragonal-to-orthorhombic structural transition at T_s and forms twin domains before ordering antiferromagnetically at T_N ($T_s \geq T_N$) [9,10]. Although spin waves throughout the Brillouin zone (BZ) have been mapped out on twinned samples, they do not allow a conclusive determination of the intrinsic magnetic exchange interactions and the origin of magnetism due to complication of the twin domain, which mixes spin waves from the twin domains at the same position in reciprocal space [4,11–14].

In this Letter, we report inelastic neutron scattering measurements of spin excitations in uniaxial-strain detwinned $BaFe_2As_2$ [15–18]. In the unstrained state, $BaFe_2As_2$ undergoes a nearly simultaneous structural and magnetic phase transition at $T_s \approx T_N \approx 138$ K from a paramagnetic tetragonal state to an AF orthorhombic state [9,10]. Below T_N, $BaFe_2As_2$ exhibits a collinear AF order [Fig. 1(a)], with an in-plane magnetic wave vector $\mathbf{Q}_{\mathrm{AF}} = (1, 0)$ [Fig. 1(b)] [9]. Because of the twinning effect, magnetic Bragg peaks appear at both $\mathbf{Q}_{\mathrm{AF}} = (\pm 1, 0)$ and $(0, \pm 1)$. Therefore, spin waves on twinned $BaFe_2As_2$ stem from both the $\mathbf{Q}_{\mathrm{AF}} = (\pm 1, 0)$ and $(0, \pm 1)$ positions, and are fourfold symmetric [11–14]. Although spin waves from twinned samples were described by a local-moment Heisenberg Hamiltonian with effective exchange couplings J_{1a}, J_{1b}, and J_2 [Fig. 1(a)] [11,13], one can hardly justify the assumption that magnetic excitations will be absent at $(0, \pm 1)$ up to the (magnetic) band top in this itinerant system. On the other hand, spin waves from the twin domains overlap at energies close to the band top and therefore make it difficult to determine if a local-moment Heisenberg Hamiltonian can faithfully describe the intrinsic spin-wave spectra of a detwinned sample.

To resolve this problem and completely determine the intrinsic spin-wave spectra of detwinned $BaFe_2As_2$, we carried out inelastic neutron scattering measurements on an assembly of mechanically detwinned $BaFe_2As_2$ single crystals, with pressure ranging from 12–22 MPa [19]. Our measurements were carried out at the MERLIN time-of-flight neutron-scattering spectrometer at the ISIS Facility, Rutherford Appleton Laboratory. The sample set was aligned with the c axis along the incident beam ($\mathbf{k_i} \| c$) direction.

Figures 1(c)–1(e) summarize the key results obtained from our measurements of the spin waves. In a completely

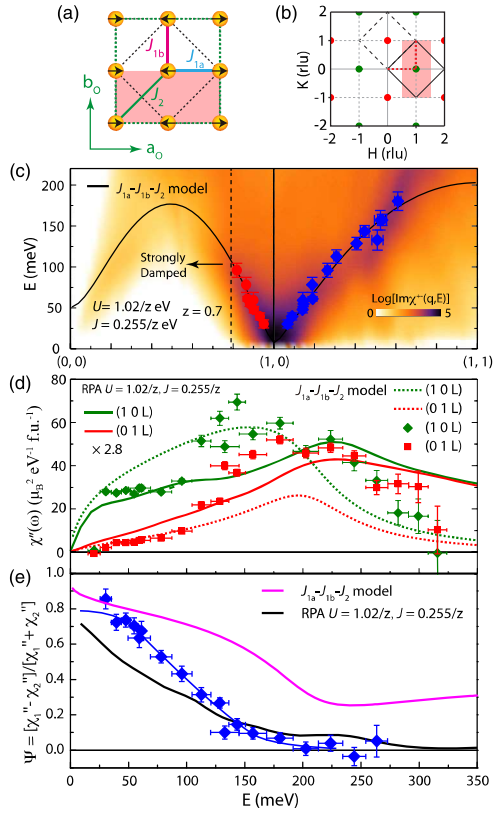

FIG. 1. Summary of neutron-scattering results and theoretical calculations of spin waves of detwinned $BaFe_2As_2$. (a) Spin arrangement of Fe^{2+} in the FeAs plane and the definition of the effective magnetic exchange couplings J_{1a}, J_{1b} and J_2. The pink area marks the AF unit cell of $BaFe_2As_2$. (b) Reciprocal space of $BaFe_2As_2$ with twin domains. The green and red dots mark the magnetic Bragg peak positions for twin domains. The pink rectangular area is the AF Brillouin zone. The black diamonds centered at (1,0) and (0,1) are the integration region for calculating energy-dependent local dynamic susceptibility. (c) Spin-wave dispersions of a detwinned $BaFe_2As_2$ extracted from constant-energy cuts collected at $T = 7$ K. The black curves are obtained from a Heisenberg model (J_{1a}-J_{1b}-J_2) fit of twinned $BaFe_2As_2$ [13]. The background shows the spectral weight from the RPA calculation (renormalized with $z = 0.7$) with $U = 1.02/z$ eV and $J = U/4$ [19]. (d) Energy-dependent local susceptibility $\chi''(E)$ for AF Brillouin zones at (1,0) and (0,1). The green and red dashed lines are spin-wave fits from a Heisenberg Hamiltonian obtained from a twinned sample (with arbitrary units) [13]. The green and red solid lines are from MF + RPA calculations, which were multiplied by 2.8 for clear comparison. (e) Spin-wave anisotropy $\psi(E)$. The purple and black solid lines are calculated spin-wave anisotropy from the Heisenberg Hamiltonian and MF + RPA, respectively. The blue line is a guide for the eye of the experimental data. The vertical error bars in (c) and horizontal error bars in (d) and (e) mark the integrating energy ranges. The vertical error bar in (c) indicates a 1σ confidential interval for the fitting of the momentum position. The ones in (d) and (e) originate from the uncertainty of the scattered neutrons and the propagation of the uncertainty for the calculation of $\chi''(E)$ and ψ, respectively.

detwinned sample, the magnetic unit cell in real space and its corresponding BZ in reciprocal space are plotted as pink regions in Figs. 1(a) and 1(b), respectively. Low-energy spin waves from the collinear AF order in Fig. 1(a) should stem from $(\pm 1, K)$ with $K = 0, \pm 2$ positions in reciprocal space [Fig. 1(b)] [17]. The red and blue data points in Fig. 1(c) show spin-wave dispersions from detwinned $BaFe_2As_2$ along the $[H, 0]$ and $[1, K]$ directions, respectively. The black solid lines are dispersion curves along the same two directions from the J_{1a}-J_{1b}-J_2 Heisenberg Hamiltonian describing spin-wave dispersions of twinned $BaFe_2As_2$ [13]. We see that the dispersion for detwinned $BaFe_2As_2$ agrees well with results from the Heisenberg fit to the twinned sample, confirming that the uniaxial pressure used to detwin the samples does not affect the magnetic interactions [25].

To further test if the Heisenberg Hamiltonian [13] can also describe the spin excitations of detwinned $BaFe_2As_2$, we consider the energy dependence of the local dynamic susceptibility, defined as $\chi''(E) = \int_{BZ} \chi''(\mathbf{Q}, E) d\mathbf{Q} / \int_{BZ} d\mathbf{Q}$, where $\chi''(\mathbf{Q}, E)$ is the wave vector and energy dependence of the imaginary part of the dynamic susceptibility within a BZ [pink rectangle or black diamond in Fig. 1(b)] [4], at the (1,0) (denoted by χ_1'') and (0,1) (denoted by χ_2'') wave vectors. For twinned $BaFe_2As_2$, $\chi_1''(E)$ equals $\chi_2''(E)$ at all energies, and spin waves exhibit C_4 rotational symmetry [13]. The green diamonds and red squares in Fig. 1(d) show the measured $\chi_1''(E)$ and $\chi_2''(E)$ in a detwinned $BaFe_2As_2$, respectively. In the present study, $\chi''(\mathbf{Q}, E)$ is calibrated using a standard vanadium sample. The averaged $\chi''(E) = [\chi_1''(E) + \chi_2''(E)]/2$ shows the same energy dependence as that for a twinned sample [13], with approximately the same intensity (within the ~30% error of the absolute intensity calibration) [19]. While the local dynamic susceptibility is dominated by $\chi_1''(E)$ for spin-wave energies below ~100 meV, $\chi_1''(E)$ and $\chi_2''(E)$ become indistinguishable for energies above 170 meV. For comparison, the dashed green and red lines are the corresponding calculated local dynamic susceptibilities using parameters obtained from fits to spin waves in a twinned sample, which have different $\chi_1''(E)$ and $\chi_2''(E)$ for all energies [13]. We see that the Heisenberg Hamiltonian fails at all energies to describe $\chi_1''(E)$ and $\chi_2''(E)$ in a detwinned $BaFe_2As_2$. In Fig. 1(e), this is shown more clearly in the energy dependence of magnetic susceptibility anisotropy, defined as $\psi(E) = [\chi_1''(E) - \chi_2''(E)]/[\chi_1''(E) + \chi_2''(E)]$. The anisotropy calculated from the Heisenberg Hamiltonian is much larger than experimental results at most energies, because spin excitations arise only from (1,0) in this picture.

Figures 2(a)–2(i) reveal the energy and wave-vector dependence of the spin excitations in detwinned $BaFe_2As_2$ measured at $T = 7$ K. Figures 2(a) and 2(c) plot the background-subtracted spin-wave scattering for $E_i = 81$ meV projected in $(\mathbf{Q}, E)$ planes with $\mathbf{Q}$ along the $[1, K]$ and $[H, 0]$ directions, respectively. Sharp spin waves

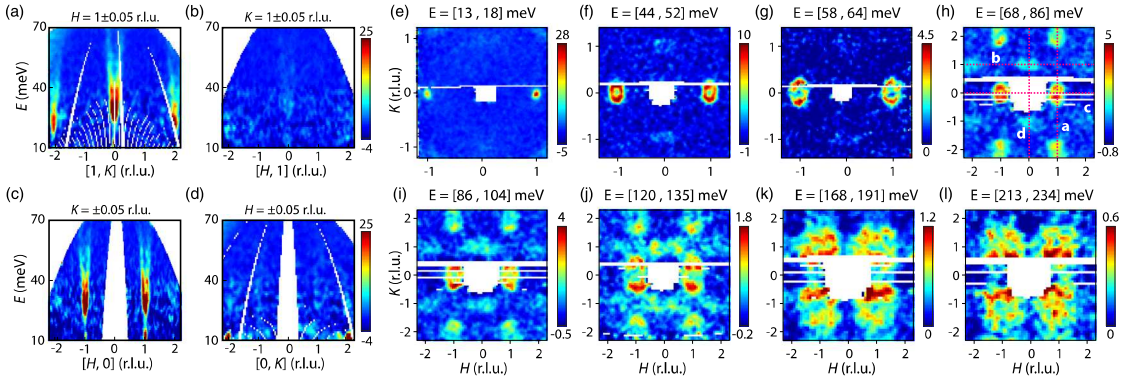

FIG. 2. Projection of the magnetic scattering intensity $((d^2\sigma/d\mathbf{\Omega}dE)(k_i/k_f))$ onto energy and momentum planes. (a)–(d) Magnon dispersions along the (a) $[1, K]$, (b) $[H, 1]$, (c) $[H, 0]$, and (d) $[0, K]$ directions measured with $E_i = 81$ meV. These four directions are marked by red dashed lines in (h). (e)–(l) Constant-energy slices in the $[H, K]$ plane. (e) is measured with $E_i = 30$ meV, (f),(g) with $E_i = 81$ meV, (h)–(j) with $E_i = 250$ meV, and (k),(l) with $E_i = 450$ meV. All the data in this figure were collected at $T = 7$ K.

are seen to originate from the AF ordering wave vectors $(1, K)$ with $K = 0, \pm 2$ [Fig. 2(a)] and $(\pm 1, 0)$ [Fig. 2(c)]. Similar projections around wave vectors $(0, \pm 1)$ yield no visible magnetic scattering at the expected twin-domain positions, confirming the nearly 100% detwinning ratio of the $BaFe_2As_2$ sample, as seen from Figs. 2(b) and 2(d). Figures 2(e)–2(l) show the two-dimensional (2D) constant-energy images of the spin excitations in the (H, K) plane at different energies. For spin-wave energies of $E = 15.5 \pm 2.5$ meV [Fig. 2(e)], 48 ± 4 meV [Fig. 2(f)], and 61 ± 3 meV [Fig. 2(g)], we see clear spin-wave rings stemming from $\mathbf{Q}_{\mathrm{AF}} = (\pm 1, 0)$ with essentially no observable scattering from the twin-domain positions $(0, \pm 1)$. For spin-wave energies at $E = 77 \pm 9$ meV [Fig. 2(h)], 97 ± 9 meV [Fig. 2(i)], and 127.5 ± 7.5 meV [Fig. 2(j)], the spin modes split along the $[1, K]$ direction, and weak spin excitations appear at the $(0, \pm 1)$ positions. Upon further increase of the energy to $E = 179.5 \pm 11.5$ meV [Fig. 1(k)] and 223.5 ± 10.5 meV [Fig. 2(l)], we can no longer identify any spin-wave anisotropy, and the excitations exhibit C_4 rotational symmetry as in a twinned sample.

To understand the data presented in Figs. 1 and 2, we model the electronic degrees of freedom with $3d$-Fe orbital character by a multiorbital Hubbard model. The hopping matrix elements describing the propagation of uncorrelated electrons are taken from the five-orbital model in Ref. [20], while the interaction Hamiltonian consists of intra- and interorbital onsite repulsion as well as Hund's coupling and a pair-hopping interaction [19]. Within the framework of a multiorbital Hubbard model, information about the magnetic fluctuations of the electronic system, as probed by inelastic neutron scattering, can be extracted from the electronic spin-spin correlation functions. Here, we determine these correlation functions within the random phase approximation (RPA) that treats the electronic system as composed of coherent quasiparticles and neglects self-energy effects beyond the mean-field level in general, and the incoherent (and potentially localized) electronic background in particular. The RPA correctly captures the stripe spin-density wave (SDW) instability in the magnetic channel driven by Fermi surface nesting between the electron and hole pockets [31]. The RPA also incorporates Landau-damping effects of the magnetic excitations due to the inclusion of decay into particle-hole pairs [32]. To account for correlation effects beyond mean-field (MF) theory, we include a phenomenological self-energy that describes both uniform band renormalization and reduced quasiparticle weight. The value of the renormalization factor z is then determined by matching the bandwidth of magnetic excitations to the experimental result. The MF + RPA data shown in Figs. 1 and 3 have been renormalized with $z = 0.7$. This value seems roughly consistent with orbitally averaged estimates from dynamical mean-field theory (DMFT) [33] ($z \approx 0.49$) and slave-spin mean-field theory [34] ($z \approx 0.43$) calculations for $BaFe_2As_2$.

To correctly capture the Goldstone mode in the magnetic channel when entering the AF phase (where we neglect the spin-rotation-symmetry-breaking effects of spin-orbit coupling that manifest only at energies less than ~30 meV [35–37]), we self-consistently stabilize a magnetic stripe configuration [21,22] with a local moment parallel to a within MF theory and by the RPA determine the magnetic fluctuations in the AF ordered state [22,32,38–40]. In presenting our results, we limit ourselves to the transverse (with respect to a spin-quantization axis chosen parallel to a) susceptibility. The longitudinal contributions give rise to small quantitative correction only [19].

Figures 3(a)–3(l) show images of our RPA results at identical energy and wave vectors to those of the experiments in Figs. 2(a)–2(l). The calculated results capture the emergence of the spin excitations at $(0, \pm 1)$ and are in reasonable agreement with magnon dispersion and the global topology of the spectral weight distribution, as shown in Figs. 1(c) and 3 [19]. Figures 2(a) and 2(c) show

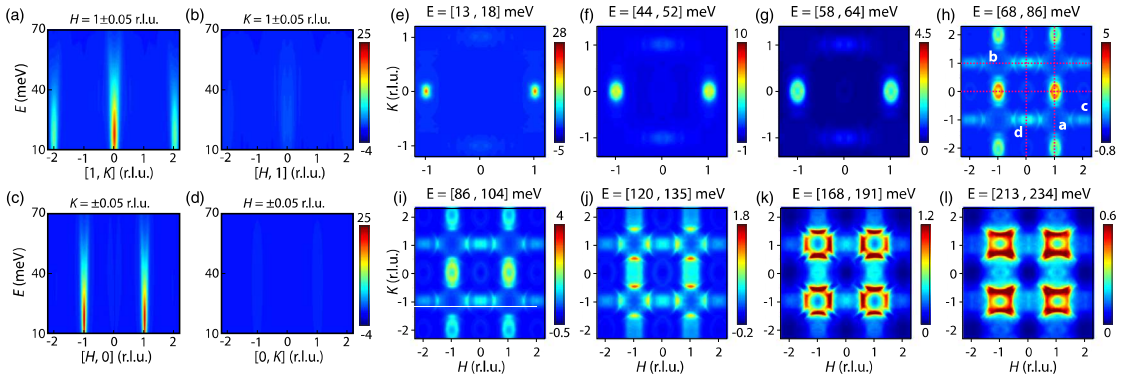

FIG. 3. Theoretical MF + RPA calculations of the magnetic scattering intensity as shown in Fig. 2 with $U = 1.02/z$ eV and Hund's coupling $J = 0.255/z$ eV ($z = 0.7$). The intensity for magnetic scattering in this figure is obtained from $\chi''(\mathbf{q}, \omega)$ calculated using MF + RPA, taking into account magnetic form factor, Bose factor, etc. [19]. To facilitate the comparison, the intensity from calculation was multiplied by a factor of 2.8.

an intensity maximum at ~30 meV because of the L modulation of the magnetic excitations, which were not included in the calculation for Fig. 3. Within the RPA, the description of the spin-wave anisotropy improves significantly over the Heisenberg result, as seen from Fig. 1(e). This consistency signals the importance of an itinerant description of the magnetic degrees of freedom in iron pnictides. While at low energies, Landau-damped spin waves at $(\pm 1, 0)$ dominate and render the spin excitation spectrum C_2 symmetric, the spin waves evolve into particle-hole-like excitations for higher energies. The presence of these transverse excitations at both $(\pm 1, 0)$ and $(0, \pm 1)$ eventually renders the high-energy part of the spectrum C_4 symmetric and gives rise to a characteristic drop in the spin-wave anisotropy that cannot be described by the Heisenberg model.

While the standard RPA approach is known to yield a too-small spectral weight (that translates to a too-small fluctuating moment) compared to experiments, we achieve qualitative agreement for the shape of the magnetic excitation spectrum by employing a phenomenological renormalization factor z, as can be seen in Fig. 1(c). We note that we cannot cure the notorious problem of too-small spectral weight in our RPA calculations by inclusion of a renormalization factor z. There is, however, evidence from work on another correlated itinerant system [41] that the inclusion of vertex corrections is necessary to accurately describe the overall intensity, while the fine structure of the frequency- and momentum-dependent susceptibility is determined by the particle-hole propagator.

In addition to spin waves, the spin-excitation anisotropy $\psi(E, T)$ above T_N in uniaxial-strained $BaFe_2As_2$ [17], which is intimately connected to the electronic nematic [42–45] and reflects the coupling between nematic susceptibility [25] and spin dynamics [17], has so far only been studied at very low energies [17]. Here, we provide results for the energy and temperature dependence of the spin-excitation anisotropy in the paramagnetic state, which is crucial for understanding the nature of the electronic nematic phase [46].

Figure 4 summarizes the temperature and energy dependence of $\psi(E, T)$. Figure 4(a) shows the temperature dependence of the spin-excitation anisotropy $\psi(E, T)$ at energies of $E = 10.6 \pm 2.8$, 15.7 ± 2.3, 61 ± 3, and 97 ± 7 meV. With increasing energy, $\psi(E, T)$ disappears at progressively lower temperatures, and essentially vanishes

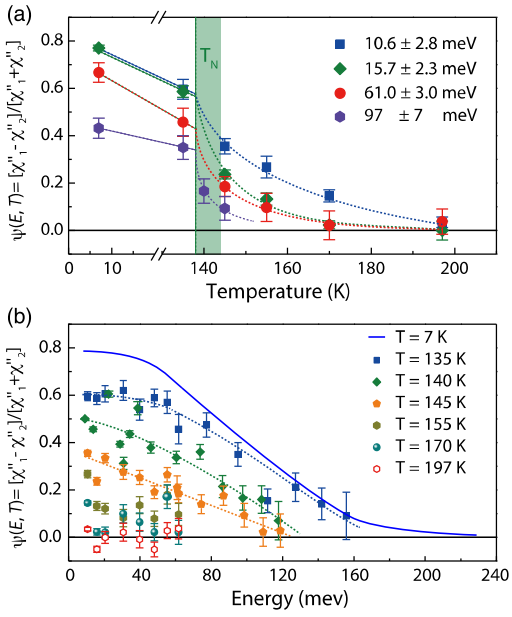

FIG. 4. Temperature and energy dependence of the nematic spin correlations of uniaxial-strained $BaFe_2As_2$. (a) Temperature dependence of the spin-excitation anisotropy (ψ) between (1,0) and (0,1) for energy transfers of 10.6 ± 2.8, 15.7 ± 2.3, 61 ± 3, and 97 ± 7 meV. (b) ψ as a function of energy transfer measured at various temperatures from 7 K to 197 K. The solid line marks the anisotropy for 7 K as shown in Fig. 1(e). The dashed lines in (a) and (b) are guides to the eye.

above T_N at $E = 97 \pm 7$ meV. Figure 4(b) shows the energy dependence of $\psi(E,T)$ at temperatures below and above T_N. At temperatures 7 K and 135 K ($<T_N$), the spin waves are anisotropic up to $E \approx 160$ meV. Upon warming up to 140 K, 145 K, 155 K, 170 K, and 197 K, the energies of spin-excitation anisotropy decrease gradually with increasing energy and become isotropic at 197 K. These results set an upper limit for the characteristic temperature for the nematic spin correlations, as well as the energy scale of the spin excitations affected by the structural nematic susceptibility [25].

In the paramagnetic phase, the MF + RPA calculation gives qualitatively similar results to DFT + dynamical mean-field theory (DMFT) calculations [6,27,47,48], where correlation effects are taken into account on a microscopic level. Since it is challenging to calculate spin waves in the AF ordered state of iron pnictides using DFT + DMFT, the MF + RPA approach allows us to explore the evolution of the spin waves to the paramagnon-like excitations across the AF transition. It turns out, however, that the RPA calculation in the paramagnetic state significantly underestimates the temperature and energy scale of the nematic spin correlations. We attribute the failure of the paramagnetic RPA calculation to capture the observed spin-excitation anisotropy ψ to neglecting the feedback of the temperature-dependent nematic order parameter onto both the electronic states and the spin excitations. Correspondingly, the nematic order parameter obtains a finite value even above T_s and therefore can affect both electronic and magnetic properties. Within a spin-nematic scenario [49], the paramagnon gap at, e.g., $(\pm 1, 0)$ will decrease, while it will increase at $(0, \pm 1)$. The nematic order will thereby increase the spin-excitation anisotropy compared to our paramagnetic RPA calculation and provide a characteristic temperature dependence.

We gratefully acknowledge the Science and Technology Facilities Council (STFC) for access to neutron beamtime at ISIS. We thank Changle Liu, Rong Yu, Qimiao Si, and Shiliang Li for helpful discussions. The work at BNU is supported by the Fundamental Research Funds for the Central Universities and the National Natural Science Foundation of China under Grant No. 11734002 (X. L.). The neutron-scattering work at Rice University was supported by U.S. National Science Foundation Grant No. DMR-1700081 (P. D.). The $BaFe_2As_2$ single-crystal synthesis work at Rice University was supported by Robert A. Welch Foundation Grant No. C-1839 (P. D.). D. D. S. and B. M. A. acknowledge financial support from the Carlsberg Foundation. Part of the work at IOP, CAS is supported by the National Natural Science Foundation of China (11374011 and 11674372) and the Youth Innovation Promotion Association of CAS (2016004). D. A. and H. L. thank the support from exchange program between the Royal Society of U.K. and National Natural Science Foundation of China (No. 11611130165).

*luxy@bnu.edu.cn
†bma@nbi.ku.dk
‡pdai@rice.edu

[1] P. A. Lee, N. Nagaosa, and X.-G. Wen, Rev. Mod. Phys. **78**, 17 (2006).
[2] B. Keimer, S. A. Kivelson, M. R. Norman, S. Uchida, and J. Zaanen, Nature (London) **518**, 179 (2015).
[3] D. J. Scalapino, Rev. Mod. Phys. **84**, 1383 (2012).
[4] P. C. Dai, Rev. Mod. Phys. **87**, 855 (2015).
[5] M. Le Tacon, G. Ghiringhelli, J. Chaloupka, M. Moretti Sala, V. Hinkov, M. W. Haverkort, M. Minola, M. Bakr, K. J. Zhou, S. Blanco-Canosa, C. Monney, Y. T. Song, G. L. Sun, C. T. Lin, G. M. De Luca, M. Salluzzo, G. Khaliullin, T. Schmitt, L. Braicovich, and B. Keimer, Nat. Phys. **7**, 725 (2011).
[6] M. Wang, C. Zhang, X. Lu, G. Tan, H. Luo, Y. Song, M. Wang, X. Zhang, E. A. Goremychkin, T. G. Perring, T. A. Maier, Z. Yin, K. Haule, G. Kotliar, and P. Dai, Nat. Commun. **4**, 2874 (2013).
[7] N. S. Headings, S. M. Hayden, R. Coldea, and T. G. Perring, Phys. Rev. Lett. **105**, 247001 (2010).
[8] R. Coldea, S. M. Hayden, G. Aeppli, T. G. Perring, C. D. Frost, T. E. Mason, S.-W. Cheong, and Z. Fisk, Phys. Rev. Lett. **86**, 5377 (2001).
[9] Q. Huang, Y. Qiu, Wei Bao, M. A. Green, J. W. Lynn, Y. C. Gasparovic, T. Wu, G. Wu, and X. H. Chen, Phys. Rev. Lett. **101**, 257003 (2008).
[10] M. G. Kim, R. M. Fernandes, A. Kreyssig, J. W. Kim, A. Thaler, S. L. Bud'ko, P. C. Canfield, R. J. McQueeney, J. Schmalian, and A. I. Goldman, Phys. Rev. B **83**, 134522 (2011).
[11] J. Zhao, D. T. Adroja, D.-X. Yao, R. Bewley, S. Li, X. F. Wang, G. Wu, X. H. Chen, J. Hu, and P. Dai, Nat. Phys. **5**, 555 (2009).
[12] S. O. Diallo, V. P. Antropov, T. G. Perring, C. Broholm, J. J. Pulikkotil, N. Ni, S. L. Budko, P. C. Canfield, A. Kreyssig, A. I. Goldman, and R. J. McQueeney, Phys. Rev. Lett. **102**, 187206 (2009).
[13] L. W. Harriger, H. Q. Luo, M. S. Liu, C. Frost, J. P. Hu, M. R. Norman, and P. Dai, Phys. Rev. B **84**, 054544 (2011).
[14] R. A. Ewings, T. G. Perring, J. Gillett, S. D. Das, S. E. Sebastian, A. E. Taylor, T. Guidi, and A. T. Boothroyd, Phys. Rev. B **83**, 214519 (2011).
[15] I. R. Fisher, L. Degiorgi, and Z. X. Shen, Rep. Prog. Phys. **74**, 124506 (2011).
[16] C. Dhital, Z. Yamani, W. Tian, J. Zeretsky, A. S. Sefat, Z. Wang, R. J. Birgeneau, and S. D. Wilson, Phys. Rev. Lett. **108**, 087001 (2012).
[17] X. Lu, J. T. Park, R. Zhang, H. Luo, A. H. Nevidomskyy, Q. Si, and P. Dai, Science **345**, 657 (2014).
[18] Y. Song, X. Lu, D. L. Abernathy, D. W. Tam, J. L. Niedziela, W. Tian, H. Luo, Q. Si, and P. C. Dai, Phys. Rev. B **92**, 180504(R) (2015).
[19] See Supplemental Material at http://link.aps.org/supplemental/10.1103/PhysRevLett.121.067002 for detailed data analysis and calculation, which includes Refs. [20–30].
[20] H. Ikeda, R. Arita, and J. Kuneš, Phys. Rev. B **81**, 054502 (2010).

[21] M. N. Gastiasoro and B. M. Andersen, Phys. Rev. B **92**, 140506(R) (2015).
[22] D. D. Scherer, I. Eremin, and B. M. Andersen, Phys. Rev. B **94**, 180405(R) (2016).
[23] A. J. Leggett, Phys. Rev. **140**, A1869 (1965).
[24] Y. Chen, X. Lu, M. Wang, H. Luo, and S. Li, Supercond. Sci. Technol. **24**, 065004 (2011).
[25] X. Lu, K. F. Tseng, T. Keller, W. Zhang, D. Hu, Y. Song, H. Man, J. T. Park, H. Luo, S. Li, A. H. Nevidomskyy, and P. Dai, Phys. Rev. B **93**, 134519 (2016).
[26] C. Lester, J.-H. Chu, J. G. Analytis, T. G. Perring, I. R. Fisher, and S. M. Hayden, Phys. Rev. B **81**, 064505 (2010).
[27] M. Liu, L. W. Harriger, H. Luo, M. Wang, R. A. Ewings, T. Guidi, H. Park, K. Haule, G. Kotliar, S. M. Hayden, and P. Dai, Nat. Phys. **8**, 376 (2012).
[28] C. Zhang, L. W. Harriger, Z. Yin, W. Lv, M. Wang, G. Tan, Y. Song, D. L. Abernathy, W. Tian, T. Egami, K. Haule, G. Kotliar, and P. Dai, Phys. Rev. Lett. **112**, 217202 (2014).
[29] H. Man, X. Lu, J. S. Chen, R. Zhang, W. Zhang, H. Luo, J. Kulda, A. Ivanov, T. Keller, E. Morosan, Q. Si, and P. Dai, Phys. Rev. B **92**, 134521 (2015).
[30] D. W. Tam, Y. Song, H. Man, S. C. Cheung, Z. Yin, X. Lu, W. Wang, B. A. Frandsen, L. Liu, Z. Gong, T. U. Ito, Y. Cai, M. N. Wilson, S. Guo, K. Koshiishi, W. Tian, B. Hitti, A. Ivanov, Y. Zhao, J. W. Lynn *et al.*, Phys. Rev. B **95**, 060505 (R) (2017).
[31] P. J. Hirschfeld, M. M. Korshunov, and I. I. Mazin, Rep. Prog. Phys. **74**, 124508 (2011).
[32] M. Kovacic, M. H. Christensen, M. N. Gastiasoro, and B. M. Andersen, Phys. Rev. B **91**, 064424 (2015).
[33] S. L. Skornyakov, A. V. Efremov, N. A. Skorikov, M. A. Korotin, Yu. A. Izyumov, V. I. Anisimov, A. V. Kozhevnikov, and D. Vollhardt, Phys. Rev. B **80**, 092501 (2009).
[34] L. de Medici, G. Giovannetti, and M. Capone, Phys. Rev. Lett. **112**, 177001 (2014).
[35] N. Qureshi, P. Steffens, S. Wurmehl, S. Aswartham, B. Büchner, and M. Braden, Phys. Rev. B **86**, 060410(R) (2012).
[36] C. Wang, R. Zhang, F. Wang, H. Luo, L. P. Regnault, P. Dai, and Y. Li, Phys. Rev. X **3**, 041036 (2013).
[37] Y. Li, W. Wang, Y. Song, H. Man, X. Lu, F. Bourdarot, and P. Dai, Phys. Rev. B **96**, 020404(R) (2017).
[38] P. M. R. Brydon and C. Timm, Phys. Rev. B **80**, 174401 (2009).
[39] J. Knolle, I. Eremin, A. V. Chubukov, and R. Moessner, Phys. Rev. B **81**, 140506(R) (2010).
[40] E. Kaneshita and T. Tohyama, Phys. Rev. B **82**, 094441 (2010).
[41] E. A. Goremychkin, H. Park, R. Osborn, S. Rosenkranz, J.-P. Castellan, V. R. Fanelli, A. D. Christianson, M. B. Stone, E. D. Bauer, K. J. McClellan, D. D. Byler, and J. M. Lawrence, Science **359**, 186 (2018).
[42] M. Yi, D. Lu, J.-H. Chu, J. G. Analytis, A. P. Sorini, A. F. Kemper, B. Moritz, S.-K. Mo, R. G. Moore, M. Hashimoto, W.-S. Lee, Z. Hussain, T. P. Devereaux, I. R. Fisher, and Z.-X. Shen, Proc. Natl. Acad. Sci. U.S.A. **108**, 6878 (2011).
[43] J. H. Chu, J. G. Analytis, K. De Greve, P. L. McMahon, Z. Islam, Y. Yamamoto, and I. R. Fisher, Science **329**, 824 (2010).
[44] J. H. Chu, H.-H. Kuo, J. G. Analytis, and I. R. Fisher, Science **337**, 710 (2012).
[45] M. Yi, Y. Zhang, Z.-X. Shen, and D. Lu, npj Quantum Mater. **2**, 57 (2017).
[46] R. M. Fernandes, A. V. Chubukov, and J. Schmalian, Nat. Phys. **10**, 97 (2014).
[47] H. Park, K. Haule, and G. Kotliar, Phys. Rev. Lett. **107**, 137007 (2011).
[48] Z. P. Yin, K. Haule, and G. Kotliar, Nat. Phys. **10**, 845 (2014).
[49] M. H. Christensen, J. Kang, B. M. Andersen, and R. M. Fernandes, Phys. Rev. B **93**, 085136 (2016).